

Phase components in Zr_7Ni_{10} and Hf_7Ni_{10} binary alloys; investigations by perturbed angular correlation spectroscopy and first principles calculations

S.K. Dey^{1,2*}, C.C. Dey^{1,2}, S. Saha^{1,2}, G. Bhattacharjee^{1,2}, D. Banerjee³, D. Toprek⁴

¹*Saha Institute of Nuclear Physics, 1/AF Bidhannagar, Kolkata-700 064, India*

²*Homi Bhabha National Institute, Anushaktinagar, Mumbai-400 094, India*

³*Accelerator Chemistry Section, RCD(BARC), Variable Energy Cyclotron Centre, Kolkata-700 064, India*

⁴*Institute of Nuclear Sciences Vinca, University of Belgrade, P. O. Box 522, 11001 Belgrade, Serbia*

Abstract

Intermetallic compounds Zr_7Ni_{10} and Hf_7Ni_{10} have been studied by perturbed angular correlation (PAC) spectroscopy considering the fact that Zr_7Ni_{10} has application as hydrogen storage material in fuel cell. In stoichiometric Zr_7Ni_{10} , the phase Zr_2Ni_7 is found to be dominant ($\sim 38\%$) while a fraction of $\sim 25\%$ is found for the Zr_7Ni_{10} phase at room temperature. In this compound, a phase due to Zr_8Ni_{21} ($\sim 10\%$) is found from room temperature up to 773 K but, this is not found at 873 K and above. In the stoichiometric Hf_7Ni_{10} sample, the phase due to Hf_7Ni_{10} is found as a minor phase ($\sim 22\%$) at room temperature. In this system, no phase of Hf_2Ni_7 is observed but, a different phase due to $HfNi_3$ is found to be dominant ($\sim 62\%$). It is found

*corresponding author

Email addresses: skumar.dey@saha.ac.in (S.K. Dey^{1,2}), chandicharan.dey@saha.ac.in (C.C. Dey^{1,2}), satyajit.saha@saha.ac.in (S. Saha^{1,2}), gourab.bhattacharjee@saha.ac.in (G. Bhattacharjee^{1,2}), dbanerjee@vecc.gov.in (D. Banerjee³), toprek@vin.bg.ac.rs (D. Toprek⁴)

that the site fraction of $\text{Hf}_7\text{Ni}_{10}$ enhances with temperature at the expense of HfNi_3 and this phase becomes predominant ($\sim 57\%$) at 673 K and above. The change of phase fractions of HfNi_3 and $\text{Hf}_7\text{Ni}_{10}$ with temperature is found to be reversible. The phase components in $\text{Zr}_7\text{Ni}_{10}$ and $\text{Hf}_7\text{Ni}_{10}$ have been determined also from X-ray powder diffraction (XRD) and transmission electron microscopy/selected area electron diffraction (TEM/SAED) measurements. Ab-initio calculations using the all electron full potential (linearized) augmented plane wave [FP-(L)APW] method, within the framework of the density functional theory (DFT), have been performed to determine the electric field gradients at the ^{181}Ta impurity sites and therefrom to assign the different components observed from PAC measurements. Present experimental and calculated results of EFG support the $Cmca$ space group for both $\text{Zr}_7\text{Ni}_{10}$ and $\text{Hf}_7\text{Ni}_{10}$ compounds.

Keywords: A. intermetallic compounds; C. ab initio calculations; C. X-ray diffraction; D. crystal structure; D. electronic structure

1. Introduction

The alloys based on Zr-Ni system have numerous technological applications. These are used as an integral part to form high temperature eutectics [1], bulk glassy alloys [2, 3], corrosion resistant material [3, 4], shape memory alloys [5], superalloys [6, 7], superconductors [8]. Magnetic properties in the transition metal based $\text{Zr}_9\text{Ni}_{11}$ alloy was found earlier [9]. Some of the Zr-Ni binary alloys, viz. $\text{Zr}_8\text{Ni}_{21}$, $\text{Zr}_7\text{Ni}_{10}$, ZrNi and $\text{Zr}_9\text{Ni}_{11}$ [10–16] have received considerable attention due to their ability to absorb large amount of gaseous hydrogen and reversibility in hydrogen dissociation process. These alloys form metal hydrides (MH) after hydrogen absorption and these MHs are used as negative electrodes in Ni-MH rechargeable batteries. The Ni-MH batteries have been widely used in hybrid electric vehicles (HEV) due to their high

energy density. Electrochemical capacity is found to be maximum for Zr_7Ni_{10} among Zr-Ni binary alloys [14]. Recently, it has been found that the hydrogenation property of TiFe alloy is improved due to the addition of small fraction of Zr_7Ni_{10} [17]. Another recent study [18] reported improvement in hydrogenation kinetics and capacity of Ti-V-Cr body centered cubic (BCC) solid solutions when Zr_7Ni_{10} was used as an additive. The Hf-Ni alloys also have many technological applications. The alloys of Ni-Ti-Hf exhibit shape memory behavior [19]. Intermetallic compounds of Hf and transition metals (Fe, Co, Pd, Pt) have also hydrogen storage properties [20], with high H/M ratio at room temperature.

Considering the above technological applications of these compounds, Zr_7Ni_{10} and Hf_7Ni_{10} binary alloys have been studied by perturbed angular correlation (PAC) spectroscopy to determine the phase components produced in the stoichiometric samples and their stabilities with temperature. To the best of our knowledge, no previous investigation in Zr_7Ni_{10} was done by PAC spectroscopy. In Hf_7Ni_{10} , however, PAC measurements were carried out by Gil et al. [21]. These authors found five electric quadrupole frequencies from PAC measurements. But, the components were not assigned by comparing with DFT calculations.

The crystal structure of Zr_7Ni_{10} was first reported to be a non-centrosymmetric orthorhombic structure with space group $Aba2$ by Kirkpatrick et al. [22]. Later on, Joubert et al. [23] corrected the crystal structure to be centrosymmetric orthorhombic structure with space group $Cmca$. The compound Hf_7Ni_{10} is reported to be isostructural with Zr_7Ni_{10} [22–24].

The perturbed angular correlation is an useful nuclear technique to study the structural properties, phase transitions, crystalline defects and magnetic ordering in intermetallic compounds [39]. In this technique, the angular correlation of a suitable γ - γ cascade of the probe nucleus is perturbed by hyperfine interaction. The nu-

clear moments (electric quadrupole moment/magnetic dipole moment) of the probe nucleus interact with hyperfine fields (electric field gradient/magnetic field) present at the probe site in the investigated sample. The electric field gradient (EFG) at the probe site is created by the surrounding charge distribution with a non-cubic symmetry and it is sensitive to the change of local electron density. Production of multiple phases in intermetallic alloys can be identified by this technique from the observation of different EFGs in the sample. Phase stability of compounds can be observed from temperature dependent PAC measurements. Internal magnetic field of a ferromagnetic material can be determined through the measurement of Larmor precession frequency. Using this technique, EFGs and magnetic ordering in Hf/Zr-Ni systems were studied earlier [25, 26, 28–33, 61]. Recently we have studied two Zr-Ni compounds which have hydrogen storage properties. These are Zr_8Ni_{21} [34], Zr_9Ni_{11} [36]. In the present report, studies in another hydrogen absorbing material viz. Zr_7Ni_{10} and its Hf analogue compound have been carried out by PAC, X-ray diffraction (XRD) and transmission electron microscopy/selected area electron diffraction (TEM/SAED) techniques.

Present investigations have been carried out to determine the phases components in these alloys. Temperature dependent PAC measurements in the range 77-1073 K have been carried out to determine the phase stability. Assignment of phases and site preference of the probe atom have been done by comparing the measured values of EFG with the calculated results by density functional theory.

2. Experimental details

The intermetallic alloys Zr_7Ni_{10} and Hf_7Ni_{10} were prepared by arc-melting high purity Hf, Zr and Ni metals in stoichiometric amounts in an argon atmosphere. These metals were procured from Alfa Aesar. The purity of Zr was $\sim 99.2\%$ excluding Hf

(maximum Hf concentration 4.5 wt%) and the purity of Hf was $\sim 99.95\%$ excluding Zr (maximum Zr concentration 3 wt%). The purity of Ni used was 99.98%. For preparation of Zr_7Ni_{10} , stoichiometric amounts of Zr and Ni were taken and melted homogeneously in the arc furnace by repeated melting. A shiny globule of Zr_7Ni_{10} was formed which was then remelted with a tiny piece (<1 at%) of natural Hf metal wire. The sample was then activated to ^{181}Hf by irradiating with thermal neutrons using a flux of $\sim 10^{13}/cm^2/s$ at Dhruva reactor, Mumbai. For preparation of Hf_7Ni_{10} , a tiny Hf metal (~ 1 at%) was first activated to ^{181}Hf . The active Hf metal sample was then remelted with the sample Hf_7Ni_{10} , prepared in the arc furnace. The probe ^{181}Hf resides at the Zr sites for Zr_7Ni_{10} sample due to their chemical and structural similarity. In Hf_7Ni_{10} , the probe replaces identical Hf atoms. These samples were then sealed in evacuated quartz tubes for PAC measurements at high temperatures. Inactive samples of Zr_7Ni_{10} and Hf_7Ni_{10} were prepared separately in the arc furnace in a similar manner for XRD and TEM/SAED measurements. The XRD measurements were carried out by TTRAX-III x-ray diffractometer (Rigaku, Japan) using the Cu K_α radiation. Transmission electron microscopy (TEM) measurements were carried out using FEI, Tecnai G2 F30, S-Twin microscope equipped with a high angle annular dark-field (HAADF) detector, a scanning unit and a energy dispersive X-ray spectroscopy (EDX) unit to perform the scanning transmission electron microscopy (STEM-HAADF-EDX).

In the PAC technique, the probe ^{181}Hf undergoes a β^- decay ($T_{1/2}=42.4$ d) to ^{181}Ta and emits two successive γ -rays of energy 133 keV and 482 keV passing through an intermediate level (482 keV) with $T_{1/2}=10.8$ ns and spin angular momentum $I = 5/2^+ \hbar$ [37]. The angular correlation of 133-482 keV γ - γ cascade is perturbed by the interaction of electric quadrupole moment ($Q=2.36$ b [38]) of the intermediate level and the surrounding EFG.

The perturbation function $G_2(t)$ for $I = 5/2 \hbar$ in a polycrystalline sample is given by [39–41],

$$G_2(t) = S_{20}(\eta) + \sum_{i=1}^3 S_{2i}(\eta) \cos(\omega_i t) \exp(-\delta \omega_i t). \quad (1)$$

The frequencies ω_i are the transition frequencies between the three sublevels of the intermediate level arising due to hyperfine splitting. The S_{2i} parameters depend on the asymmetry of the electric field gradient and these are expressed as a polynomial in asymmetry parameter (η). Due to lattice strain or defects present in a real crystal, the probe may get displaced from the actual lattice site. Different probes are thus subjected to slightly different electronic and ionic environment in the same phase of the crystal. This effect is considered by an exponential (Lorentzian) distribution function where δ is mean frequency distribution width. A least squares fitting to eqn. (1) determines the quadrupole frequency (ω_Q) through the observed transition frequencies ω_1 , ω_2 and ω_3 . In the principal axis system, the EFG tensor has zero off-diagonal elements. Conventionally, the largest component of the EFG tensor is designated as V_{zz} which is related to quadrupole frequency by

$$\omega_Q = \frac{eQV_{zz}}{4I(2I-1)\hbar}. \quad (2)$$

The principal EFG components (V_{xx} , V_{yy} and V_{zz}) obey the Laplace's equation

$$V_{xx} + V_{yy} + V_{zz} = 0, \quad \text{where} \quad |V_{zz}| \geq |V_{yy}| \geq |V_{xx}|. \quad (3)$$

The symmetry of the EFG is determined by the asymmetry parameter η , defined as

$$\eta = \frac{V_{xx} - V_{yy}}{V_{zz}}, \quad \text{where} \quad 0 \leq \eta \leq 1. \quad (4)$$

Therefore, EFG can be determined from only two parameters V_{zz} and η . For $\eta = 0$, the perturbation function becomes periodic and harmonic, and the quadrupole

frequency is related to the transition frequencies (ω_i) by

$$\omega_Q = \omega_1/6 = \omega_2/12 = \omega_3/18. \quad (5)$$

When $\eta \neq 0$, the perturbation function remains periodic but not harmonic. The relations between ω_Q and ω_i become more complex and can be found in the reference [41].

Present PAC measurements have been carried out using a four detector BaF₂-BaF₂ or a four detector LaBr₃(Ce)-BaF₂ PAC set up. The crystal sizes were 38.1(dia) \times 25.4(ht) mm² for LaBr₃(Ce) and 50.8(dia) \times 50.8(ht) mm² for BaF₂. In the LaBr₃(Ce)-BaF₂ setup, the 133 keV γ -rays were selected in the LaBr₃(Ce) detector. Standard slow-fast coincidence assemblies were formed to collect data at 180° and 90° [42]. Typical prompt time resolutions (FWHM) of \sim 1 ns and \sim 790 ps were obtained at ¹⁸¹Hf energy window settings for the BaF₂-BaF₂ and LaBr₃(Ce)-BaF₂ setup, respectively. Details of experimental set up and data analysis can be found in reference [42].

3. Results and discussion

3.1 Zr₇Ni₁₀

The XRD powder pattern obtained in stoichiometric Zr₇Ni₁₀ sample is shown in Figure 1. Peaks were first identified using ICDD database. The presence of orthorhombic Zr₇Ni₁₀ ([23], PDF Card No.: 01-072-3501), triclinic Zr₈Ni₂₁ ([43], PDF Card No.: 01-071-2622) and monoclinic Zr₂Ni₇ ([44], PDF Card No.: 01-071-0543) phases have been found from XRD analysis. The x-ray intensity profile has been fitted using FullProf software package [45]. The presence of Zr₇Ni₁₀, Zr₂Ni₇ and Zr₈Ni₂₁ phases in this stoichiometric sample of Zr₇Ni₁₀ have been observed from TEM/SAED measurement also (Figure 2). The SAED pattern obtained from a

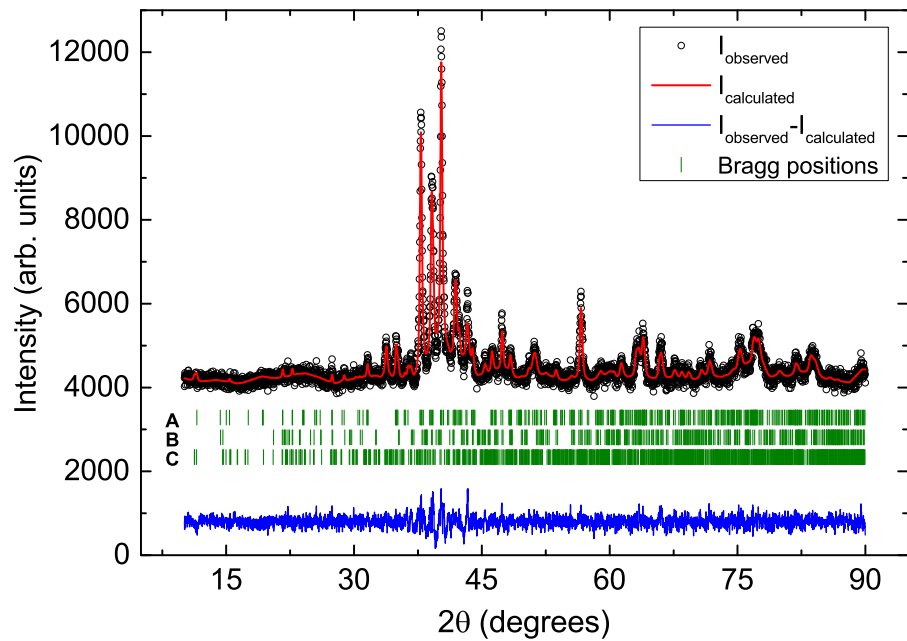


Figure 1: The background subtracted XRD powder pattern in the stoichiometric sample of Zr_7Ni_{10} . The vertical bars A, B and C denote the Bragg angles corresponding to Zr_7Ni_{10} , Zr_2Ni_7 and Zr_8Ni_{21} phases, respectively.

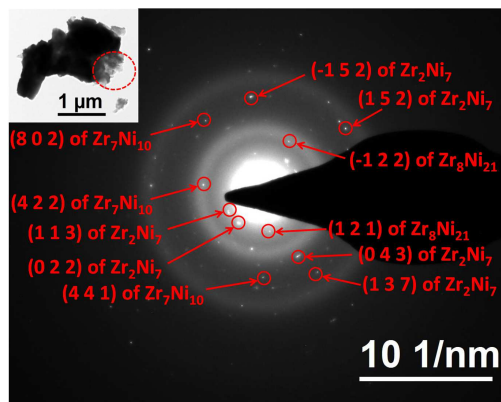


Figure 2: Selected area electron diffraction pattern from stoichiometric Zr_7Ni_{10} particle shown in the inset.

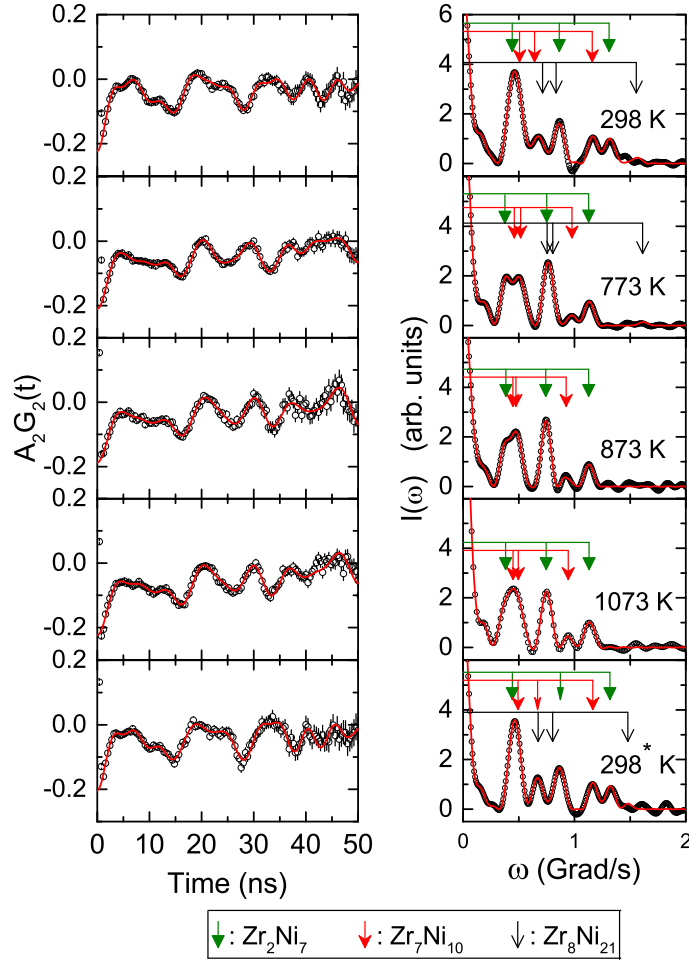


Figure 3: Perturbed angular correlation spectra in $\text{Zr}_7\text{Ni}_{10}$ at different temperatures. Left panel shows the time spectra and the right panel shows the corresponding Fourier cosine transforms. The PAC spectrum designated by 298* K is taken at room temperature after the measurement at 1073 K.

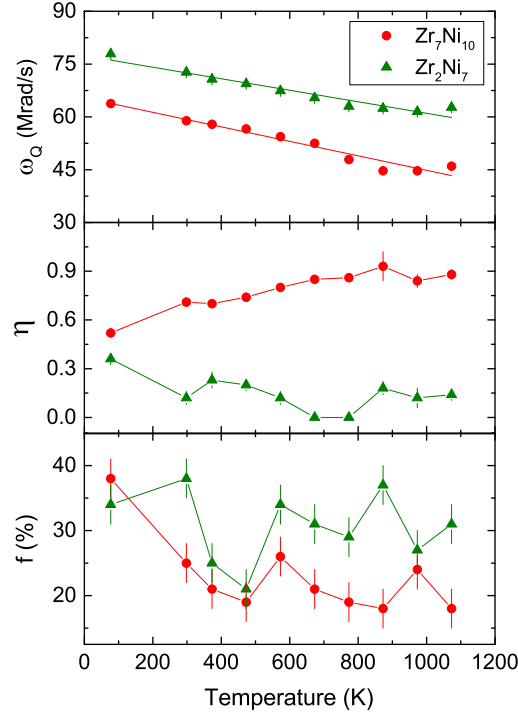


Figure 4: Variations of quadrupole frequency (ω_Q), asymmetry parameter (η) and site fraction f (%) with temperature for the components of Zr_7Ni_{10} and Zr_2Ni_7 .

region marked by a dotted circle in the stoichiometric sample of Zr_7Ni_{10} is shown in Figure 2. The interplaner spacing (d_{hkl}) is obtained by measuring the distance (Δq) of a particular spot from the central bright spot using the formula $d_{hkl} = 1/\Delta q$. Few of the measured d_{hkl} from the SAED pattern are 1.47(4) Å, 2.26(4) Å and 1.81(4) Å. These measured interplaner spacings are very close to the (8 0 2), (4 2 2) and (4 4 1) inter-planer spacings of orthorhombic Zr_7Ni_{10} (ICDD PDF Card No.:01-072-3501), respectively. This further confirms the presence of Zr_7Ni_{10} phase in the sample. Some of the measured d_{hkl} from the SAED pattern are 1.39(4) Å, 1.49(4) Å, 2.73(4) Å, 3.39(4) Å, 1.83(4) Å and 1.36(4) Å which are very close to the (-1 5 2), (1 5

2), (1 1 3), (0 2 2), (0 4 3) and (1 3 7) inter-planer spacings of monoclinic Zr_2Ni_7 (JCPDS # 65-2321), respectively. The presence of Zr_2Ni_7 phase in the sample is thus confirmed. Few of the measured interplaner spacings from the SAED pattern, 2.34(4) Å and 3.38(4) Å, are found to be very close to the (-1 2 2) and (1 2 1) inter-planer spacing of triclinic $\text{Zr}_8\text{Ni}_{21}$ (ICDD PDF Card No.: 01-071-2622), respectively, which confirms the presence of $\text{Zr}_8\text{Ni}_{21}$ phase in the stoichiometric sample of $\text{Zr}_7\text{Ni}_{10}$.

The PAC spectrum in the stoichiometric $\text{Zr}_7\text{Ni}_{10}$ sample at room temperature is shown in Figure 3. The spectrum is found to be best fitted by considering five quadrupole frequencies. Texture effects are observed in the sample which indicates that the EFGs produced at the probe sites are not randomly oriented and it is not a perfect polycrystalline sample. Therefore, the spectrum is analyzed using free S_{2n} ($n=0,1,2,3$) parameters. At room temperature, a major component ($\sim 38\%$) is found with values of $\omega_Q = 72.7(3)$ Mrad/s, $\eta = 0.12(4)$ and $\delta = 1.1(7)\%$. This component can be assigned to Zr_2Ni_7 by comparing with the results found in Zr_2Ni_7 [31]. In the stoichiometric ZrNi_3 [35] and ZrNi_5 [32] alloys also, the phase Zr_2Ni_7 was produced as a major component.

The second major component (Table 1) with values of $\omega_Q = 58.9(3)$ Mrad/s, $\eta = 0.71(1)$ is attributed to $\text{Zr}_7\text{Ni}_{10}$ phase by comparing the result with our DFT calculation (discussed later). A minor component ($\sim 11\%$) was found to be present with values of $\omega_Q = 77.1(9)$ Mrad/s, $\eta = 0.81(2)$. This component has been identified as $\text{Zr}_8\text{Ni}_{21}$ by comparing the result with our recent PAC investigation in $\text{Zr}_8\text{Ni}_{21}$ [34] for Zr(1) crystallographic site. Apart from these components, two other minor frequency components (Table 1) have been found. These two components are attributed to defects. Since the activation of the sample was done after preparing the sample, crystalline defects can be produced by neutron irradiation [46]. From the Zr-Ni phase diagram, it is found that the phase Zr_2Ni_7 melts congruently and $\text{Zr}_8\text{Ni}_{21}$ phase is

formed peritectically from Zr_2Ni_7 and liquid melt ($\text{L} + \text{Zr}_2\text{Ni}_7 \rightarrow \text{Zr}_8\text{Ni}_{21}$) at 1453 K [47]. The phases $\text{Zr}_7\text{Ni}_{10}$ and $\text{Zr}_8\text{Ni}_{21}$ are formed from liquid alloy by an eutectic reaction ($\text{L} \rightarrow \text{Zr}_8\text{Ni}_{21} + \text{Zr}_7\text{Ni}_{10}$) [47] at 1333 K. The phase $\text{Zr}_7\text{Ni}_{10}$ is also formed by peritectic reaction from $\text{Zr}_9\text{Ni}_{11}$ and liquid melt ($\text{L} + \text{Zr}_9\text{Ni}_{11} \rightarrow \text{Zr}_7\text{Ni}_{10}$) at 1393 K [48].

At 77 K, the Zr_2Ni_7 and $\text{Zr}_7\text{Ni}_{10}$ phases were found only (Table 1). All the three Zr-Ni phases, viz. Zr_2Ni_7 , $\text{Zr}_8\text{Ni}_{21}$ and $\text{Zr}_7\text{Ni}_{10}$ are present in the temperature range 298-773 K (Table 1). At 873 K and above, the component due to $\text{Zr}_8\text{Ni}_{21}$ does not appear. The phases Zr_2Ni_7 and $\text{Zr}_7\text{Ni}_{10}$, however, remain stable up to 1073 K. The phase Zr_2Ni_7 is found to be predominant in the whole temperature range (77-1073 K) among the Zr-Ni binary phases that are produced in the stoichiometric sample of $\text{Zr}_7\text{Ni}_{10}$. The frequency values for the fourth and fifth components show anomalous temperature dependence (Table 1). This further indicates that these components are irregular defect components. A re-measurement is carried at room temperature after measurement at 1073 K. Here, all the three Zr-Ni phases, viz. Zr_2Ni_7 , $\text{Zr}_7\text{Ni}_{10}$ and $\text{Zr}_8\text{Ni}_{21}$ produced with almost same fractions reversibly.

Temperature evolution of quadrupole frequency, asymmetry parameter and site fraction for two Zr-Ni phases, viz. Zr_2Ni_7 and $\text{Zr}_7\text{Ni}_{10}$ present in the stoichiometric sample of $\text{Zr}_7\text{Ni}_{10}$ are shown in Figure 4. The asymmetry parameter of $\text{Zr}_7\text{Ni}_{10}$ phase is found to increase with temperature. The quadrupole frequencies for both the components decrease linearly with temperature. The values of quadrupole frequencies obtained for Zr_2Ni_7 and $\text{Zr}_7\text{Ni}_{10}$ phases in the temperature range 77-1073 K have been fitted with the following relation

$$\omega_Q(T) = \omega_Q(0)[1 - \alpha T]. \quad (6)$$

The fitted results give $\omega_Q(0) = 65(1)$ Mrad/s ($V_{zz} = 7.3(2) \times 10^{21}$ V/m²), $\alpha =$

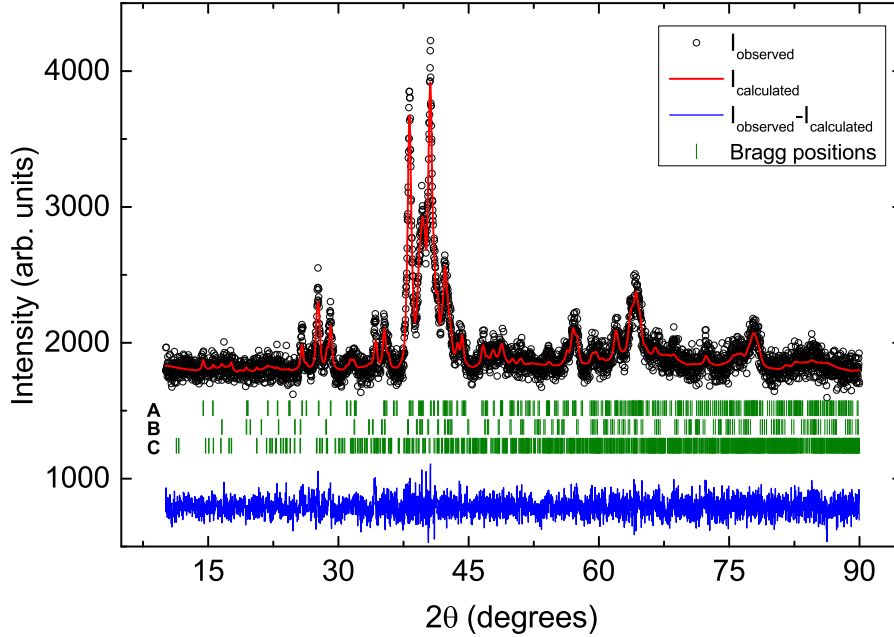


Figure 5: The background subtracted XRD powder pattern in the stoichiometric sample of $\text{Hf}_7\text{Ni}_{10}$. The vertical bars A, B and C denote the Bragg angles corresponding to $\text{Hf}_7\text{Ni}_{10}$, $\beta\text{-HfNi}_3$ and $\text{Hf}_8\text{Ni}_{21}$, respectively.

$3.1(3) \times 10^{-4} \text{ K}^{-1}$ for $\text{Zr}_7\text{Ni}_{10}$ component. For the Zr_2Ni_7 component, the results are $\omega_Q(0) = 77(1) \text{ Mrad/s}$ ($V_{zz} = 8.6(2) \times 10^{21} \text{ V/m}^2$), $\alpha = 2.1(2) \times 10^{-4} \text{ K}^{-1}$. The linear temperature dependence of quadrupole frequency was observed in many intermetallic compounds [25, 49–54].

3.2 $\text{Hf}_7\text{Ni}_{10}$

The XRD powder pattern in the $\text{Hf}_7\text{Ni}_{10}$ sample is shown in Figure 5. The peaks were identified using ICDD database, 2009. Presence of the hexagonal $\beta\text{-HfNi}_3$ ([55], PDF Card No.: 01-071-0475), orthorhombic $\text{Hf}_7\text{Ni}_{10}$ [22], and triclinic $\text{Hf}_8\text{Ni}_{21}$ ([56], PDF Card No.: 01-071-0476) phases are found in the stoichiometric $\text{Hf}_7\text{Ni}_{10}$

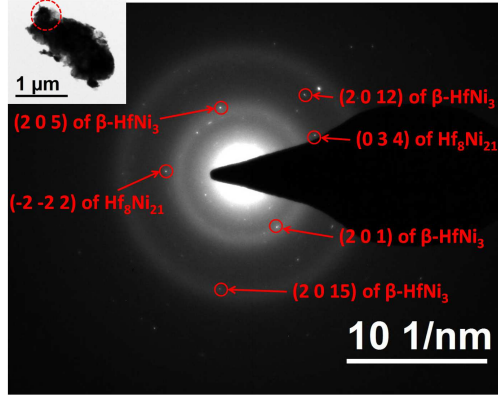


Figure 6: Selected area electron diffraction pattern from stoichiometric $\text{Hf}_7\text{Ni}_{10}$ particle shown in the inset.

sample. Fitting of the XRD intensity profile has been carried out using FullProf software package [45]. The space group for $\text{Hf}_7\text{Ni}_{10}$ has been considered $Cmca$ due to its isostructurality with $\text{Zr}_7\text{Ni}_{10}$ [22, 24]. Selected area electron diffraction (SAED) pattern obtained from a region marked by a dotted circle in the stoichiometric sample of $\text{Hf}_7\text{Ni}_{10}$ is shown in Fig. 6. Some of the measured interplaner spacing from the SAED pattern are $1.41(4) \text{ \AA}$, $2.27(4) \text{ \AA}$ and $2.01(4) \text{ \AA}$ which are found to be very close to the $(2\ 0\ 12)$, $(2\ 0\ 1)$ and $(2\ 0\ 5)$ inter-planer spacings of hexagonal $\beta\text{-HfNi}_3$ (JCPDS #71-0475). This further confirms the presence of HfNi_3 phase in the sample. Few of the interplaner spacing from the SAED pattern are $1.70(4) \text{ \AA}$ and $1.82(4) \text{ \AA}$. These are found to be very close to the $(0\ 3\ 4)$ and $(-2\ -2\ 2)$ interplaner spacings of triclinic $\text{Hf}_8\text{Ni}_{21}$ (JCPDS #71-0476). The phase $\text{Hf}_7\text{Ni}_{10}$ could not be identified from SAED pattern in the stoichiometric sample of $\text{Hf}_7\text{Ni}_{10}$ due to non-availability of x-ray diffraction data of interplaner spacings (d_{hkl}) and corresponding crystallographic planes ($h\ k\ l$) for $\text{Hf}_7\text{Ni}_{10}$.

The PAC spectrum at room temperature in the stoichiometric $\text{Hf}_7\text{Ni}_{10}$ sample is

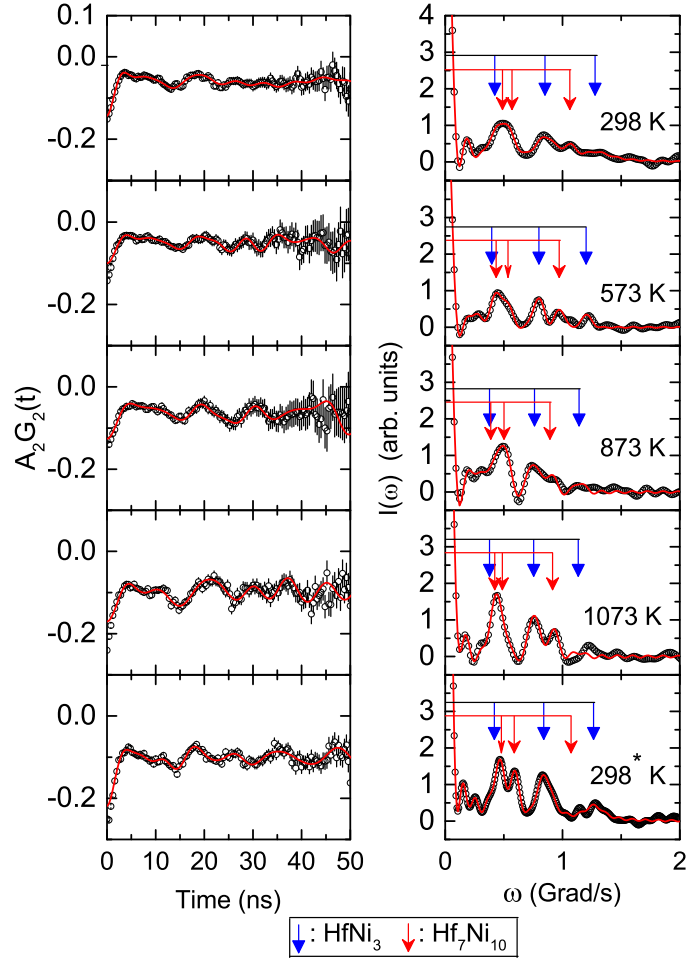


Figure 7: Time differential perturbed angular correlation spectra in $\text{Hf}_7\text{Ni}_{10}$ at different temperatures. Left panel shows the time spectra and the right panel shows the corresponding Fourier cosine transforms. The PAC spectrum designated by 298* K is taken at room temperature after the measurement at 1073 K.

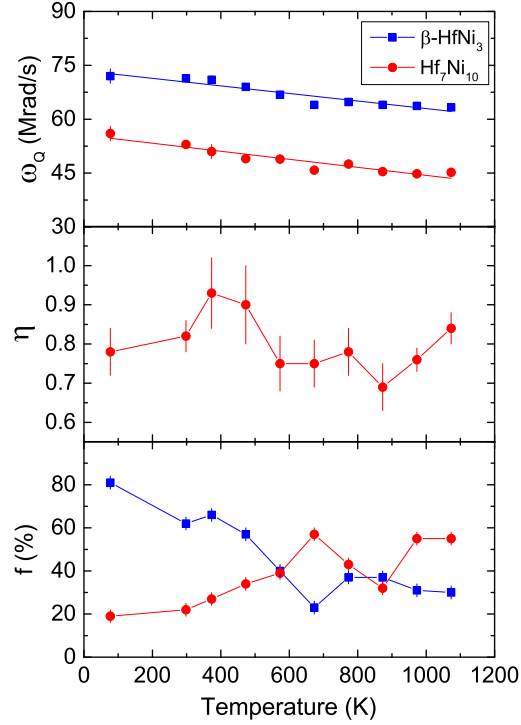


Figure 8: Variations of quadrupole frequency (ω_Q), asymmetry parameter (η) and site fraction $f(\%)$ with temperature for the components of $\text{Hf}_7\text{Ni}_{10}$ and $\beta\text{-HfNi}_3$.

shown in Figure 7. Fitting of the spectrum shows the presence of three quadrupole frequency components. Analysis of the spectrum has been carried out using free S_{2n} ($n=0,1,2,3$) parameters as the sample is found to have texture effects. The predominant component ($\sim 62\%$) produces values of $\omega_Q = 71.4(9)$ Mrad/s, $\eta = 0$, $\delta = 11(2)\%$. This component has been assigned to $\beta\text{-HfNi}_3$ by comparing the values with the results from our recent PAC investigation in HfNi_3 sample [35] for Hf(3) crystallographic site. The second component produces values of $\omega_Q = 53(1)$ Mrad/s, $\eta = 0.82(4)$ with site fraction $\sim 22\%$. This component has been assigned to $\text{Hf}_7\text{Ni}_{10}$ by comparing the values with the results found in the analogous $\text{Zr}_7\text{Ni}_{10}$ phase (Table 1) and with the results from DFT calculations (discussed later). A

minor component ($\sim 16\%$) with values of $\omega_Q = 32(1)$ Mrad/s, $\eta = 0$ was also found to be present. The value of quadrupole frequency for this component varies with temperature in an irregular manner and suggests that this is a crystalline defect produced during sample preparation. In the PAC sample, however, no component due to $\text{Hf}_8\text{Ni}_{21}$ was observed. In the Hf-Ni phase diagram, it is found that Hf_2Ni_7 and HfNi are congruently melting phases. The HfNi_3 has two polymorphs, one is high temperature phase ($\alpha\text{-HfNi}_3$) which is stable above 1473 K and the other is low temperature phase ($\beta\text{-HfNi}_3$) which is stable below 1473 K [57]. The phase HfNi_3 is produced by peritectic reaction of liquid melt with Hf_2Ni_7 ($\text{L} + \text{Hf}_2\text{Ni}_7 \rightarrow \text{HfNi}_3$) at 1573 K. It was reported [58] that the phase $\text{Hf}_7\text{Ni}_{10}$ is produced by peritectic reaction $\text{L} + \text{Hf}_9\text{Ni}_{11} \rightarrow \text{Hf}_7\text{Ni}_{10}$ [58] at ~ 1563 K. At 77 K, the phase fraction of $\beta\text{-HfNi}_3$ component enhances to $\sim 81\%$. The site fraction of $\text{Hf}_7\text{Ni}_{10}$ increases while the site percentage of $\beta\text{-HfNi}_3$ phase decreases up to 673 K (Figure 8) with the increase of temperature. However, the phase $\beta\text{-HfNi}_3$ was found to be predominant up to 573 K (Table 2). The $\text{Hf}_7\text{Ni}_{10}$ phase becomes predominant ($\sim 57\%$) and the phase fraction of $\beta\text{-HfNi}_3$ decrease to 23% at 673 K. In the temperature range 773-873 K, the phase fraction of $\text{Hf}_7\text{Ni}_{10}$ decreases and $\beta\text{-HfNi}_3$ increases to 37%. Major contribution ($\sim 55\%$) in the PAC spectrum at 973 K and 1073 K was found due to the $\text{Hf}_7\text{Ni}_{10}$ phase and $\beta\text{-HfNi}_3$ phase fraction reduces to $\sim 30\%$. The PAC measurement was carried out at room temperature after measurement at 1073 K. Similar results of phase fractions of $\beta\text{-HfNi}_3$ and $\text{Hf}_7\text{Ni}_{10}$ at initial room temperature and after 1073 K (Table 2) show phase reversibility of the two phases.

Variation of quadrupole frequency (ω_Q), asymmetry parameter (η) and phase fraction with temperature for $\beta\text{-HfNi}_3$ and $\text{Hf}_7\text{Ni}_{10}$ phases are shown in Figure 8. The quadrupole frequency for $\beta\text{-HfNi}_3$ and $\text{Hf}_7\text{Ni}_{10}$ phases decrease linearly with temperature following the Eqn. 6. Similar temperature dependence of ω_Q was found

in $\text{Zr}_7\text{Ni}_{10}$ which shows isostructurality of $\text{Zr}_7\text{Ni}_{10}$ and $\text{Hf}_7\text{Ni}_{10}$. The fitted results are $\omega_Q(0) = 55.9(9)$ Mrad/s ($V_{zz}=6.2(2)\times 10^{21}$ V/m²), $\alpha = 2.0(2)\times 10^{-4}$ K⁻¹ for the $\text{Hf}_7\text{Ni}_{10}$ phase. For β - HfNi_3 phase, the fitted results are $\omega_Q(0) = 73.5(9)$ Mrad/s ($V_{zz}=8.2(2)\times 10^{21}$ V/m²), $\alpha = 1.5(1)\times 10^{-4}$ K⁻¹.

4. DFT calculations and results

$\text{Zr}_7\text{Ni}_{10}$ and $\text{Hf}_7\text{Ni}_{10}$ crystallize in the orthorhombic base-centered centrosymmetric *Cmca* type structure (space group number 64) with lattice parameters $a=12.381$ Å, $b=9.185$ Å and $c=9.221$ Å for $\text{Zr}_7\text{Ni}_{10}$ [23] and $a=12.275$ Å, $b=9.078$ Å, $c=9.126$ Å for $\text{Hf}_7\text{Ni}_{10}$ [24]. This structure contains 34 atoms in the unit cell and possesses 7 non-equivalent crystallographic positions; 4 non-equivalent positions for Zr (or Hf) and 3 non-equivalent positions for Ni.

First we have optimized these structural parameters. The first-principles density functional theory (DFT) calculations were performed to compare with the experimental results. All the calculations were done using the full potential (linearized) augmented plane waves method [FP-(L)APW], as implemented in WIEN2k [59]. The energy convergence has been achieved by expanding the basis function up to $R_{MT} \cdot K_{max}=7$, where R_{MT} is the smallest atomic sphere radius in the unit cell and K_{max} gives the magnitude of the largest \vec{k} vector in the plane wave expansion. In our calculations the muffin-tin radii for Zr, Ni and Hf(Ta) were 2.2, 2.1 and 2.15 a. u., respectively. The valence wave functions inside the spheres are expanded up to $l_{max}=10$ while the charge density is Fourier expanded up to $G_{max}=16$. The energy to separate core and valence states was set to -7 Ry. Electronic exchange-correlation energy was treated with generalized gradient approximation (GGA) parametrized by Perdew-Burke-Ernzerhof (PBE) [60]. Taking into consideration both the accuracy and the efficiency of the calculations, we have selected a $8\times 8\times 8$ k point mesh to

sample the entire Brillouin-zone (BZ), yielding 143 points in the irreducible Brillouin-zone. The structure was relaxed according to Hellmann-Feynman forces calculated at the end of each self-consistent cycle, until the forces acting on all atoms were less than $0.068 \text{ eV}/\text{\AA}$ (5 mRy/a.u.). The relaxation method is described in Ref. [61]. In our calculations the self-consistency was achieved by demanding the convergence of the integrated charge difference between last two iterations to be smaller than $10^{-5}e$. All the calculations refer to zero temperature.

The theoretically optimized lattice parameters a , b and c , and fractional coordinates of atoms together with the present and previous experimental values [23, 24] are presented in Table 3. From Table 3 it can be seen that our calculated parameters are in very good agreement with the experimental results. After obtaining the optimized structural parameters, we replaced one of the host sites; i.e. one of the 4 non-equivalent positions of Zr (or Hf) by a Ta atom (preserving the point group symmetry around original atom), in order to simulate a dopant in the crystal lattice. This substitutional structures have been marked as X1-Ta, X2-Ta, X3-Ta and X4-Ta; X=Zr, Hf. For each case of the substitutional structure, we have repeated calculations again, keeping all parameters and charge convergence criteria same as in the case of the pure compounds. For example, to simulate PAC measurements at Zr1 position, we replaced one atom at position (0, 0.31359, 0.18707) with Ta atom. We checked that the two Ta atoms are sufficiently far from each other ($\sim 8 \text{ \AA}$) to avoid significant impurity-impurity interactions. The calculated electric field gradients (EFGs) in the pure compounds as well as at Ta probe positions in the $\text{Zr}_7\text{Ni}_{10}$ and $\text{Hf}_7\text{Ni}_{10}$ structures along with the values of asymmetry parameter η , are given in Table 4. The sign of EFG (V_{zz}) can not be determined from PAC measurement. Thus, absolute values of measured EFG (extrapolated to 0 K) and asymmetry parameter (at 77 K) for $\text{Zr}_7\text{Ni}_{10}$ and $\text{Hf}_7\text{Ni}_{10}$ have been compared with the theoretical

results in the Table 4. The calculation of EFG were performed by using the method developed in Ref. [62]; which is implemented in WIEN2k code. All the calculations refer to zero temperature.

We see that the calculated result for EFG at the Ta probe site replacing Zr3 atom (6.99×10^{21} V/m²) with asymmetry parameter 0.54 is in excellent agreement with the measured value of EFG extrapolated to 0 K ($7.3(2) \times 10^{21}$ V/m²) and η (77 K)=0.52(1) for the component Zr₇Ni₁₀, thus confirming that the mentioned component of the measured PAC spectra originates from Zr₇Ni₁₀. Similarly, the calculated result for EFG at the Ta probe site replacing Hf3 atom (6.37×10^{21} V/m²) with asymmetry parameter 0.77 is in excellent agreement with the measured value of EFG extrapolated to 0 K ($6.2(2) \times 10^{21}$ V/m²) and η (77 K)=0.78(6) for the component Hf₇Ni₁₀, thus confirming that the mentioned component of the measured PAC spectra originates from Hf₇Ni₁₀.

5. Conclusion

In stoichiometric Zr₇Ni₁₀ sample, the phases Zr₂Ni₇, Zr₇Ni₁₀ and Zr₈Ni₂₁ are produced where Zr₂Ni₇ is found as a major phase and a minor phase due to Zr₈Ni₂₁ is found at room temperature. In the stoichiometric Hf₇Ni₁₀ sample, the phases β -HfNi₃ and Hf₇Ni₁₀ are produced where the phase β -HfNi₃ is predominant at room temperature. The phase fraction of Hf₇Ni₁₀ increases with temperature at the expense of β -HfNi₃. At temperatures $\geq 400^\circ\text{C}$, the phase Hf₇Ni₁₀ becomes predominant which indicates that it is a high temperature phase. However, these phase fractions are found to be reversible with temperature. Similar values of quadrupole frequency and asymmetry parameter indicate isostructurality of Zr₇Ni₁₀ and Hf₇Ni₁₀ phases. In both Zr₇Ni₁₀ and Hf₇Ni₁₀, four non-equivalent crystallographic sites of Zr/Hf have been found. Our experimental results of EFG and η are in excellent agreement with

the values of EFG at ^{181}Ta sites corresponding to Zr3/Hf3 positions calculated by the first-principles density functional theory based on the full potential (linearized) augmented plane waves method [FP-(L)APW]. The origin of observed EFG in these materials can thus be explained.

Acknowledgement

The authors thankfully acknowledge Mr. A. Karmahapatra of Saha Institute of Nuclear Physics, Kolkata for X-ray diffraction measurements. The present work is supported by the Department of Atomic Energy, Government of India through the Grant no. 12-R&D-SIN-5.02-0102 and by The Ministry of Education, Science and Technological Department of the Republic of Serbia through the Grant no. 171001.

References

- [1] Chandrasekhar Tiwary, Vilas V. Gunjal, Dipankar Banerjee, and Kamanio Chattopadhyay, MATEC Web of Conferences 14 (2014) 01005.
- [2] Y. Yokoyama, K. Fujita, A.R. Yavari and A. Inoue, Philosophical Magazine Letters 89 (2009) 322.
- [3] S.J. Pang, T. Zhang, K. Asami, Mat. Trans. 43 (2002) 1771.
- [4] Daniela Zander, Uwe Köster, Materials Science and Engineering A 375-377 (2004) 53.
- [5] Matthew Carl, Jesse D. Smith, Brian Van Doren and Marcus L. Young, Metals 7 (2017) 511.

- [6] J. Zhang and R.F. Singer, Metallurgical and Materials Transactions A 35A (2004) 1337.
- [7] V. Ivanchenko, T. Kosorukova, M. Samohin, S. Samohin, Yu. Butenko, Patent of Ukraine on useful model 26254 (2007).
- [8] Saad Alzahrani and Mahmud Khan, AIP Advances 7 (2017) 055706.
- [9] V. Provenzano, R.D. Shull, R.M. Waterstrat, L.H. Bennett, E. Della Torre and H. Seyoum, IEEE Trans. Magnetics 46 (2010) 502.
- [10] J.-M. Joubert, M Latroche, A. Percheron-Guégan, J. Alloys Compd. 231 (1995) 494.
- [11] F.C. Ruiz, E.B. Castro, S.G. Real, H.A. Peretti, A. Visintin, W.E. Triaca, Int. J. Hydrogen Energy 33 (2008) 3576.
- [12] J. Nei, K. Young, R. Regmi, G. Lawes, S.O. Salley, K.Y.S. Ng, Int. J. Hydrogen Energy 37 (2012) 16042.
- [13] Kwo Young, Taihei Ouchi, Michael A. Fetcenko, Willy Mays, Benjamin Reichman, Int. J. Hydrogen Energy 34 (2009) 8695.
- [14] Kwo-hsiung Young and Jean Nei, Materials 6 (2013) 4574.
- [15] F.C. Ruiz, E.B. Castro, H.A. Peretti, A. Visitin, Int. J. Hydrogen Energy 35 (2010) 9879.
- [16] K. Young, J. Nei, T. Ouchi, M.A. Fetcenko, J. Alloys Compd. 509 (2011) 2277.
- [17] Pragya Jain, N. Skryabina, D Fruchart, J. Huot, J Alloys Compd 636 (2015) 375.

- [18] Amol Kamble, Pratibha Sharma, Jacques Huot, *Int. J. Hydrogen Energy* 43 (2018) 7424-7429.
- [19] X.L. Meng, Y.D. Fu, W. Cai, Q.F. Li and L.C. Zhao, *Phil. Mag. Lett.* 89 (2009) 431.
- [20] A. Baudry, P. Boyer, L.P. Pontonnier, *J. Phys. Condens. Matt.* 4 (1992) 5025.
- [21] J.M. Gil, B. Costa, P. de Rango, D. Fruchart, S. Miraglia, N. Skryabina, *Solid State Phenomena* 170 (2011) 293.
- [22] M.E. Kirkpatrick, J.F. Smith, W.L. Larsen, *Acta Cryst.*, 15 (1962) 894.
- [23] J.-M. Joubert, R. Černý, K. Yvon, M. Latroche, A. Percheron-Guégan, *Acta Crystallogr. C* 53 (1997) 1536.
- [24] P. Nash, A. Nash, *Bulletin of Alloy Phase Diagrams* 4 (1983) 250.
- [25] B. Wodniecka, M. Marszałek, P. Wodniecki, A.H. Hryniewicz, *Hyperfine Interact.* 80 (1993) 1039.
- [26] A.N. Poynor, S.E. Cumblidge, R.L. Rasera, G.L. Catchen, A.T. Mota, *Hyperfine Interact.* 136/137 (2001) 549.
- [27] A. Umícević, B. Čekić, V. Ivanovski, V. Koteski, J. Belošević-Čavor, M. Šiljegović, S. Pavlović, *J. Alloys Compd.* 475 (2009) 38.
- [28] B. Čekić, A. Umícević, V. Ivanovski, V. Koteski, J. Belošević-Čavor, S. Pavlović, *J. Alloys Compd.* 480 (2009) 40.
- [29] M. Marszałek, H. Saitovitch, P.R.J. Silva, *Z. Naturforsch.* 55a (2000) 49.

- [30] P.R.J. Silva, H. Saitovitch, J.T. Cavalcante, M. Forker, *J. Magn. Magn. Mater.* 322 (2010) 1841.
- [31] C.C. Dey, S.K. Srivastava, *Physica B* 427 (2013) 126.
- [32] C. C. Dey, *J. Mag. Mag. Materials* 342 (2013) 87.
- [33] C.C. Dey, Rakesh Das, S.K. Srivastava, *J. Phys. Chem. Solids* 82 (2015) 10.
- [34] S.K. Dey, C.C. Dey, S. Saha, J. Belošević-Čavor, *Intermetallics* 84 (2017) 112.
- [35] S.K. Dey, C.C. Dey, S. Saha, J. Belošević-Čavor, D. Toprek, *J. Alloys Compd.* 723 (2017) 425.
- [36] S.K. Dey, C.C. Dey, S. Saha, J. Belošević-Čavor, D. Toprek (Communicated, Arxiv Id: 2100990).
- [37] R. B. Firestone, V. S. Shirley (Eds.), *Table of Isotopes*, 8th ed., John Wiley and Sons, New York, 1996.
- [38] T. Butz, A. Lerf, *Phys. Lett. A* 97 (1983) 217.
- [39] G. Schatz, A. Weidinger, *Nuclear condensed matter physics, Nuclear Methods and Application*, John Wiley and Sons, Chichester, New York, Brisbane, Toronto, Singapore, 1996, p. 63 (chapter 5).
- [40] R. Béraud, I. Berkes, J. Danière, G. Marest and R. Rougny, *Nuclear Instruments and Methods*, 69 (1969) 41-44.
- [41] M. Zacate and H. Jaeger, *Defect Diffus. Forum* 311 (2011) 3.
- [42] C. C. Dey, *Pramana* 70 (2008) 835.

- [43] J.-M. Joubert, R. Černý, K. Yvon, M. Latroche, A. Percheron-Guégan, Z. Krist. New Cryst. Struct. 213 (1998) 227.
- [44] F.R. Eshelman, J.F. Smith, Acta Cryst. B28 (1972) 1594.
- [45] J. Rodríguez-Carvajal, Phys. B 192 (1993) 55.
- [46] Cong Dai, Peyman Saidi, Zhongwen Yao, Mark R. Daymond, Acta Materialia, 140 (2017) 56.
- [47] P. Nash, C.S. Jayanth, Bulletin of Alloy Phase Diagrams 5 (1984) 144.
- [48] T. Kosorukova, V. Ivanchenko, G. Firstov and H. Noël, Solid State Phenomena, 194 (2012) 14.
- [49] P. Wodniecki, B. Wodniecka, A. Kulińska, M. Uhrmacher, K.P. Lieb, Journal of Alloys and Compounds 312 (2000) 17-24.
- [50] B. Wodniecka, M. Marszałek, P. Wodniecki, H. Saitovitch, P.R.J. da Silva, A.Z. Hrynkiewicz, J. Alloys Comp. 219 (1995) 132.
- [51] P. Wodniecki, B. Wodniecka, M. Marszałek, A.Z. Hrynkiewicz, Z. Naturforsch. 51a (1996) 437.
- [52] P. Wodniecki, B. Wodniecka, A. Kulińska, A.Z. Hrynkiewicz, Z. Naturforsch. 53a (1997) 355.
- [53] P. Wodniecki, A. Kulińska, B. Wodniecka, A.Z. Hrynkiewicz, Z. Naturforsch. 53a (1997) 349.
- [54] H.M. Petrilli, M. Marszałek, H. Saitovitch, Z. Naturforsch. 51 (1996) 437.

- [55] Lars Bsenko, *Acta Cryst.* B34 (1978) 3201.
- [56] Lars Bsenko, *Acta Cryst.* B34 (1978) 3204.
- [57] Lars Bsenko, *J. Less-Common Metals*, 63 (1979) 171.
- [58] Z. Kejun, J. Zhanpeng, *J. Less-Common Met.* 166 (1990) 21.
- [59] P. Blaha, K. Schwarz, G.K.H. Madsen, D. Kvasnicka and J. Luitz, *WIEN2k an Augmented Plane Wave Plus Local Orbitals Program for Calculating Crystal Properties*, Vienna University of Technology, Vienna, Austria, 2001.
- [60] (a) J.P. Perdew, K. Burke and M. Ernzerhof, *Generalized Gradient Approximation Made Simple*, *Phys. Rev. Lett.* 77 (1996) 3865.
(b) J.P. Perdew, K. Burke and M. Ernzerhof, *Generalized Gradient Approximation Made Simple*, *Phys. Rev. Lett.* 77 (1996) 3865. Erratum *Phys. Rev. Lett.* 78 (1997) 1396
(c) Y. Zhang and W. Yang, *Phys. Rev. Lett.* 80 (1998) 890.
- [61] J. Belošević-Čavor, V. Koteski and J. Radaković, *Solid State Communications* 152 (2012) 107-1075.
- [62] P. Blaha, K. Schwarz and P. Herzig, *Phys. Rev. Lett.* 54 (1985) 1192.

Table 1: Results of PAC measurements in $\text{Zr}_7\text{Ni}_{10}$

Temperature (K)	Component	ω_Q (Mrad/s)	η	δ (%)	f (%)	Specification
77	1	77.9(3)	0.36(2)	0.9(6)	34(3)	Zr_2Ni_7
	2	63.8(3)	0.52(1)	0	38(3)	$\text{Zr}_7\text{Ni}_{10}$
	3	8.0(4)	0	0	28(3)	
298	1	72.7(3)	0.12(4)	1.1(7)	38(3)	Zr_2Ni_7
	2	58.9(3)	0.71(1)	0	25(3)	$\text{Zr}_7\text{Ni}_{10}$
	3	77.1(9)	0.81(2)	0	11(3)	$\text{Zr}_8\text{Ni}_{21}$
	4	8.0(7)	0	0	17(3)	
	5	33(1)	0	0	9(3)	
373	1	70.7(5)	0.23(5)	0	25(3)	Zr_2Ni_7
	2	57.9(3)	0.70(2)	0	21(3)	$\text{Zr}_7\text{Ni}_{10}$
	3	79(1)	0.81(5)	0	13(3)	$\text{Zr}_8\text{Ni}_{21}$
	4	6.7(3)	0	0	28(3)	
	5	32.7(8)	0	0	13(3)	
473	1	69.4(2)	0.20(3)	0	21(3)	Zr_2Ni_7
	2	56.6(2)	0.74(1)	0	19(3)	$\text{Zr}_7\text{Ni}_{10}$
	3	80(1)	0.82(4)	0	10(3)	$\text{Zr}_8\text{Ni}_{21}$
	4	5.7(2)	0	0	32(3)	
	5	32.3(5)	0	0	17(3)	
573	1	67.4(2)	0.12(4)	0	34(3)	Zr_2Ni_7
	2	54.4(3)	0.80(1)	0	26(3)	$\text{Zr}_7\text{Ni}_{10}$
	3	80(1)	0.82(4)	0	7(3)	$\text{Zr}_8\text{Ni}_{21}$
	4	7.7(5)	0	0	24(3)	
	5	34(1)	0	0	9(3)	
673	1	65.4(2)	0	0	31(3)	Zr_2Ni_7
	2	52.5(5)	0.85(2)	0	21(3)	$\text{Zr}_7\text{Ni}_{10}$
	3	77(1)	0.87(4)	0	7(3)	$\text{Zr}_8\text{Ni}_{21}$
	4	5.9(3)	0	0	30(3)	
	5	32.9(9)	0	0	11(3)	
773	1	63.0(2)	0	1.2(4)	29(3)	Zr_2Ni_7
	2	47.9(4)	0.86(1)	0	19(3)	$\text{Zr}_7\text{Ni}_{10}$
	3	77(1)	0.96(7)	0	8(3)	$\text{Zr}_8\text{Ni}_{21}$
	4	5.3(2)	0	0	29(3)	
	5	31.7(5)	0	0	15(3)	
873	1	62.4(2)	0.18(4)	0	37(3)	Zr_2Ni_7
	2	44.7(9)	0.93(9)	0	18(3)	$\text{Zr}_7\text{Ni}_{10}$
	3	5.5(3)	0	0	31(3)	
	4	30(1)	0	0	13(3)	
973	1	61.5(2)	0.12(6)	0	27(3)	Zr_2Ni_7
	2	44.7(7)	0.84(4)	0	24(3)	$\text{Zr}_7\text{Ni}_{10}$
	3	4.0(2)	0	0	31(3)	
	4	28.4(8)	0	0	17(3)	
1073	1	62.7(1)	0.14(3)	0	31(3)	Zr_2Ni_7
	2	46.0(5)	0.88(3)	0	18(3)	$\text{Zr}_7\text{Ni}_{10}$
	3	4.6(1)	0	0	35(3)	
	4	29.9(5)	0	0	15(3)	
298*	1	73.1(3)	0.12(7)	0	35(3)	Zr_2Ni_7
	2	59.8(7)	0.65(4)	0	31(3)	$\text{Zr}_7\text{Ni}_{10}$
	3	74(1)	0.79(5)	0	10(3)	$\text{Zr}_8\text{Ni}_{21}$
	4	7.3(6)	0	0	17(3)	
	5	32(2)	0	0	6(3)	

* After measurement at 1073 K

Table 2: Results of PAC measurements in $\text{Hf}_7\text{Ni}_{10}$

Temperature (K)	Component	ω_Q (Mrad/s)	η	δ (%)	f (%)	Specification
77	1	72(2)	0	11(3)	81(3)	β -HfNi ₃
	2	56(2)	0.78(6)	0	19(3)	Hf ₇ Ni ₁₀
298	1	71.4(9)	0	11(2)	62(3)	β -HfNi ₃
	2	53(1)	0.82(4)	0	22(3)	Hf ₇ Ni ₁₀
	3	32(1)	0	0	16(3)	
373	1	71(1)	0	7(2)	66(3)	β -HfNi ₃
	2	51(2)	0.93(9)	0	27(3)	Hf ₇ Ni ₁₀
	3	38(4)	0	0	7(3)	
473	1	69(1)	0	8(3)	57(3)	β -HfNi ₃
	2	49(1)	0.9(1)	0	34(3)	Hf ₇ Ni ₁₀
	3	33(3)	0	0	9(3)	
573	1	66.8(6)	0	0	40(3)	β -HfNi ₃
	2	48.9(9)	0.75(7)	0	39(3)	Hf ₇ Ni ₁₀
	3	42(2)	0	0	21(3)	
673	1	64.0(8)	0	0	23(3)	β -HfNi ₃
	2	45.8(6)	0.75(6)	0	57(3)	Hf ₇ Ni ₁₀
	3	45(2)	0	0	20(3)	
773	1	64.8(7)	0	0	37(3)	β -HfNi ₃
	2	47.5(7)	0.78(6)	0	43(3)	Hf ₇ Ni ₁₀
	3	39(2)	0	0	20(3)	
873	1	64.0(1)	0	0	37(3)	β -HfNi ₃
	2	45.4(6)	0.69(6)	0	32(3)	Hf ₇ Ni ₁₀
	3	40(2)	0	0	30(3)	
973	1	63.7(4)	0	0	31(3)	β -HfNi ₃
	2	44.8(4)	0.76(3)	0	55(3)	Hf ₇ Ni ₁₀
	3	16(3)	0	0	14(3)	
1073	1	63.3(4)	0	0	30(3)	β -HfNi ₃
	2	45.2(5)	0.84(4)	0	55(3)	Hf ₇ Ni ₁₀
	3	10(1)	0	0	15(3)	
298*	1	70.5(4)	0	7(1)	58(3)	β -HfNi ₃
	2	53.9(4)	0.76(1)	0	25(3)	Hf ₇ Ni ₁₀
	3	15.9(9)	0	0	16(3)	

* After measurement at 1073 K

Table 3: The lattice constants a , b and c (given in Å) of the Zr_7Ni_{10} and Hf_7Ni_{10} $Cmca$ crystal structure and the fractional coordinates of 7 crystallographic non-equivalent positions.

	Present calculated results (WIEN2k)	Experimental results [23], [24] (XRD)	Present experimental results (XRD)
Zr_7Ni_{10}			
a	12.365	12.381	12.374
b	9.172	9.185	9.173
c	9.197	9.221	9.213
Zr1	0 0.31359 0.18707	0 0.31219 0.18847	
Zr2	1/4 0.25466 1/4	1/4 0.25466 1/4	
Zr3	0.30754 0 0	0.30634 0 0	
Zr4	0 0 0	0 0 0	
Ni1	0.14438 0.01115 0.20822	0.14438 0.01115 0.20822	
Ni2	0.35507 0.29157 0.00833	0.35507 0.29157 0.00833	
Ni3	0 0.10655 0.39553	0 0.10755 0.39423	
Hf_7Ni_{10}			
a	12.281	12.275	12.279
b	9.062	9.078	9.071
c	9.151	9.126	9.120
Hf1	0 0.31439 0.1867	0 0.31219 0.18847	
Hf2	1/4 0.25504 1/4	1/4 0.25466 1/4	
Hf3	0.30645 0 0	0.30634 0 0	
Hf4	0 0 0	0 0 0	
Ni1	0.14391 0.00998 0.20874	0.14438 0.01115 0.20822	
Ni2	0.35507 0.29111 0.00665	0.35507 0.29157 0.00833	
Ni3	0 0.10699 0.39569	0 0.10755 0.39423	

Table 4: The calculated and experimental EFG values in units of 10^{21} V/m² and asymmetry parameter (η) values for Zr₇Ni₁₀ and Hf₇Ni₁₀ *Cmca* crystal structure.

Probe	Lattice Site site	calculated EFG	calculated η	Measured EFG	Measured η (77 K)
Zr ₇ Ni ₁₀					
no probe	Zr1	1.11	0.63		
(pure compound)	Zr2	4.05	0.10		
	Zr3	-3.02	0.37		
	Zr4	-3.38	0.41		
¹⁸¹ Ta	Zr1-Ta	1.33	0.77		
	Zr2-Ta	10.11	0.10		
	Zr3-Ta	-6.99	0.54	7.3(2)	0.52(1)
	Zr4-Ta	-10.75	0.25		
Hf ₇ Ni ₁₀					
no probe	Hf1	-1.15	0.33		
(pure compound)	Hf2	9.48	0.18		
	Hf3	-4.96	0.82		
	Hf4	-8.94	0.32		
¹⁸¹ Ta	Hf1-Ta	1.87	0.25		
	Hf2-Ta	9.75	0.10		
	Hf3-Ta	-6.37	0.77	6.2(2)	0.78(6)
	Hf4-Ta	-10.68	0.22		